Assessment of mine hunting performance evaluation parameters across multiple side-looking sonar systems and frequencies

Marc Geilhufe*, Warren A. Connors†, Stig. A. V. Synnes*, Øivind Midtgaard*,
Torstein O. Sæbø*, Roy E. Hansen* and Samantha Dugelay†
*Norwegian Defence Research Establishment (FFI)
PO Box 25, 2027 Kjeller, Norway
Email: marc.geilhufe@ffi.no
†NATO STO Centre for Maritime Research and Experimentation (CMRE)
Viale San Bartolomeo 400, 19126 La Spezia, Italy

***Abstract*—The adoption of autonomous underwater vehicles equipped with high-resolution side-looking sonars in mine countermeasures (MCM) operations has resulted in a requirement to quantify the effectiveness of these platforms; e. g., by the probability of correctly detecting and classifying mines along with the associated false alarm rate. Recently, the Norwegian Defence Research Establishment (FFI) proposed a performance model based on a combination of parameters given *a priori* and measured *in situ*, resulting in a through-the-sensor approach to performance evaluation for the detection and classification part of MCM operations. In this paper we investigate whether these parameters are consistent across different sonar systems and frequencies. This is done on basis of data from the MANEX'14 sea trial off the coast of Levanto, Italy, which was organized by the Centre for Maritime Research and Experimentation (CMRE). This unique data set spans five different frequency bands with carrier frequencies at 25 kHz, 72.5 kHz, 100 kHz, 300 kHz and 900 kHz, gathered from two synthetic aperture sonar systems (CMRE's MUSCLE and FFI's HISAS) as well as a real aperture sidescan sonar system.**

I. Introduction

Recent advances in sensing and robustness for autonomous underwater vehicles (AUV) have resulted in their application for naval mine countermeasures (MCM) missions. The incorporation of robotic platforms into the MCM 'toolbox' of NATO nations has provided either an effective force multiplication capability for existing MCM platforms, or a means to gain an MCM capability at a considerably lower cost than a traditional, highly specialized vessel.

The employment of both the platforms and the sensors, however, requires re-consideration of measures of effectiveness for the data products resulting from an MCM mission. Recent work has applied a through-the-sensor approach to performance evaluation for side-looking sensors, separating the performance evaluation into two major components, a sensor-centric image quality measure which considers the sensors ability to 'see' the seafloor, and an image based complexity metric which considers how difficult the environment is to detect and classify mines [1].

The MANEX'14 (Multi-national AutoNomy EXperiment 2014) [2] trial was organized by the NATO Science and Technology Organization (STO) Centre for Maritime Research and Experimentation (CMRE), and run on the NATO research vessel (NRV) Alliance off the coast of Levanto in Italy. During the experiment, the Norwegian Defence Research Establishment (FFI) and CMRE gathered high resolution seafloor and target imagery using three different vehicle/sensor combinations over the same areas. These platforms included the FFI HUGIN HUS AUV with the HISAS synthetic aperture sonar (SAS), CMRE's MUSCLE AUV using the MUSCLE SAS and CMRE's REMUS 100 AUV with a real aperture sidescan sonar (SSS).

The main sensor in AUV-based search for seabed mines is typically a side-looking sonar, either SSS or SAS. The information content and interpretation of the sonar images are, however, dependent of the acoustic frequency, the imaging geometry and the ocean environment [3], [4]. In a previous study [5], frequency related differences were explored. In this paper, we investigate the usability of the suggested performance parameters on data at different frequencies.

The remainder of this paper is as follows. Section II presents FFI's performance model and parameters, while the MANEX'14 experiment and the sonar data used in this study, are described in sections III and IV, respectively. Sections V and VI present results for the two major performance parameters and section VII discusses our findings. Finally, the paper is summarized in section VIII.

II. MCM performance estimation

Reliable performance estimates are essential for both planning and evaluation of MCM operations. The total performance depends on the success rates from all phases of the mine hunting operation. AUV-mounted side-looking sonar systems can be used for initial mine search of the operation area. Their effectiveness can be quantified by the probability of correctly detecting and classifying mines (P_{dc}), together with the associated false alarm rate (non-mine contacts). This performance depends on the environment, mine type and complete survey system (including sensor, platform, sensing configuration, data processing and data analysis system). The littoral environment varies significantly in both space and time, and affects the performance through many factors: seafloor type, water depth,

978-0-933957-43-5 ©2015 MTS

sea state, seafloor roughness, currents, clutter density, etc. Complete and accurate environmental information is rarely available prior to a mine hunting operation and predictions may be uncertain. *In situ* sensor data is thus required for post-mission assessment of the performance actually achieved, as well as for in-mission adaptation of the AUV plan to meet the targeted performance.

FFI has proposed a performance model for AUV-based mine hunting, combining through-the-sensor estimation with *a priori* information, and implemented the model into the MCM Insite tool [1]. The model was originally developed for Kongsberg's HISAS 1030, but is also applicable for other SAS and SSS models. The performance model contains two main parameters: *image quality* and *image complexity*, that are calculated from several sub-parameters, as shown in Fig. 1. Both parameters are significantly affected by the local environment, and thus require *in situ* measurements for reliable estimation.

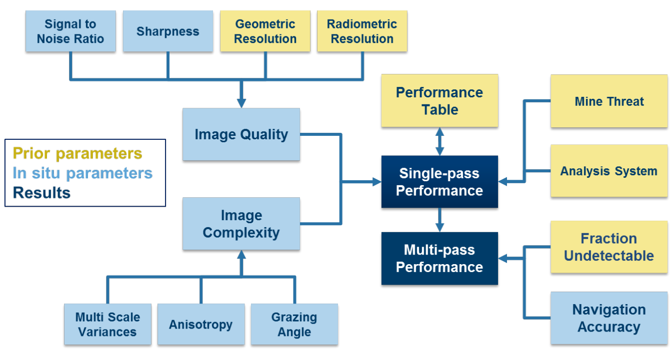

Fig. 1. Performance evaluation model used in FFI's MCM Insite tool [1]

A. Image quality parameter

Generally, following FFI's model in Fig. 1, *image quality* is defined as the product of four metrics: *Theoretical geometric resolution*, *sharpness*, *radiometric resolution* and *generalized signal-to-noise ratio (SNR)*. All of these four metrics are mapped to a value between zero and one using the Sigmoid function, thus the image quality also becomes a value between zero (low quality) and one (high quality) [1].

The *sharpness* is a function of the platform stability and will typically be lower in turns or when running with crab (due to currents) [6]. Since all data examples presented are from close to linear tracks we have chosen to omit the *sharpness* in this paper. Additionally we have chosen to omit the *theoretical geometric resolution* and the *radiometric resolution* in this study.

The *signal-to-noise ratio* in a sonar image can be estimated from a normalized sonar coherence γ as

$$\mathrm{SNR} = \frac{|\gamma|}{1 - |\gamma|}. \quad (1)$$

For an interferometric sonar, the interferometric coherence, i.e. the similarity between the signals on the different receiver arrays, is the natural metric [7], [8]. HISAS uses interferometric coherence from the real aperture to estimate the SNR. This estimate has a 3.2 m resolution across-track (this is the length of the correlation window and is a processing parameter) and a range and frequency dependent resolution along-track (e. g., the HISAS HF resolution is linearly increasing from 0.6 m at 50 m range to 2.5 m at 200 m range). However, the HISAS coherence is always estimated in a $0.5\,\mathrm{m} \times 1\,\mathrm{m}$ grid.

An alternative is to use the temporal coherence in micro-navigation; i. e., the similarity between signals from succeeding pings [9]. For a non-interferometric system, this is also the only alternative. MUSCLE uses temporal coherence as input to the SNR estimation. The across-track resolution is determined by the length of the correlation window also for this measure. However, the along-track resolution is significantly lower. For single-element DPCA [10] the resolution is N times lower, where N is the number of elements in each receiver array; for HISAS $N = 32$ and for MUSCLE's primary array $N = 36$. The MUSCLE coherence is estimated in a $0.5\,\mathrm{m} \times 7\,\mathrm{m}$ grid. Although this resolution could be increased, this would have the undesirable effect of increasing the processing load during SAS processing throughout the data collection and processing phases. Using this coherence as a parameter in the quality model will result in a lower resolution quality measurement than using interferometric coherence, as the value used is consistent throughout the entire bin.

For both coherence estimates the most dominant noise source when the sonar is operated in shallow areas is surface multipath [11]. Thus we sometimes use the term signal-to-multipath ratio rather than the SNR. However, as long as a noise-source is incoherent between the arrays or the succeeding pings, it will degrade the estimate.

B. Image complexity parameter

Following the model displayed in Fig. 1, the parameter *image complexity* is driven by the sub-parameters *multiscale variance*, *anisotropy* and *grazing angle*. In this work, we focus on the first two sub-parameters as they are the ones which depend on the environment. *Multiscale variance* is intended to describe image texture at various scales, where high values occur in areas with large contrast, e. g. caused by highlight and shadow regions of mine-size objects, and low values on homogeneous patches, for example benign seafloor. *Anisotropy* is created to capture texture patterns having a dominant orientation like in sand ripples. The idea is to distinguish between randomly oriented seafloor structure like typical cluttered areas and seafloor patches with a clear orientation like sand ripples. Both types contribute to the complexity in an image of the seabed, but to a varying degree. The information of the presence of oriented texture sand ripples as captured by the anisotropy parameter will be helpful for ATR, where a target detection and classification algorithm specialized on sand ripples could be used. On the other hand, randomly cluttered seafloor provides more challenges and thus should get rated as more complex than anisotropic areas. Hence our *image complexity* is based on *multiscale variance* but adjusted for the influence of *anisotropy* [12].

Both estimates take values between 0 and 1. They are calculated using local wavelet variances of the Maximal Overlap Discrete Wavelet Transform (MODWT) [13] at various mine-size scales. While *multiscale variance* is compound of the sum of horizontal, vertical and diagonal wavelet variances, *anisotropy* uses ratios of horizontal and vertical wavelet variances as well as 45° rotated versions of the filters (see [12] for more details). During this study we only use Haar filters with unit level filter length of two, though in principle any filters from the Daubechies class (see, e. g. [14], [13]) could be used.

III. MANEX'14 SEA TRIAL

The MANEX'14 sea trial was arranged from 22 September to 13 October 2014, on the CMRE's research vessel NRV Alliance. The experiment included participants from 10 different organizations, and employed four different autonomous vehicles [2]. The primary focus of the trial was to evaluate various approaches to autonomous perception and adaptive behaviors in a mine countermeasures context, as well as examining sensor performance on various seafloor and target types. The trial was situated off the Italian coastline from Framura to Bonassola, near Levanto in Liguria. Fig. 2 illustrates the overall trials area.

The trial was conducted using multiple AUVs equipped with synthetic aperture sonar and real aperture sidescan sonar sensors. Of primary interest in this work was the data collected from the FFI's HUGIN AUV, CMRE's MUSCLE AUV and CMRE's REMUS 100 AUV, which are shown in Fig. 3.

The HUGIN AUV, developed by Kongsberg Maritime and FFI has a diameter of 75 cm and is equipped with HISAS 1030 [15], an two-sided interferometric SAS system that generates high-resolution imagery and bathymetry of the seafloor. HISAS usually operates with a frequency band of 30 kHz centered at 100 kHz, and a nominal range of 200 m to each side for a platform speed of 2 m/s. On FFI's own vehicle HUGIN HUS, however, an additional low frequency transmitter has been mounted and the high frequency band has been extended down to 60 kHz [16]. This configuration enables experimentation at various frequency bands, where the following three were used during MANEX'14: 12-38 kHz (HISAS LF), 60-85 kHz (HISAS MF) and 85-115 kHz (HISAS HF). As HISAS LF and MF were logged simultaneously in a combined mode, their data recording range was reduced to 92 m.

The MUSCLE AUV is a medium sized Bluefin 21" (0.53 m) AUV equipped with a Thales Underwater Systems SAS with interferometric capability. This system is the primary AUV employed in MCM research at CMRE [17], and employs SAS processing software which was developed by CMRE and implemented on the vehicle using graphics processing units for real-time data processing. The MUSCLE system uses a 60 kHz frequency band at a carrier frequency of 300 kHz, and has a nominal range of 150 m.

The REMUS 100 is a lightweight AUV platform, developed by Kongsberg (Hydroid). The AUV is 1.6 m in length, with a diameter of 0.19 m, and is equipped with a Marine Sonic sidescan sonar [18]. This sonar has a dual frequency capability of 900 or 1800 kHz with variable ranges, however for this study only the 900 kHz data and a 30 m range is considered.

These vehicles were employed in a series of missions over a set of defined areas with differing seafloor types, and water depths from 19 to 30 m. The seafloor types included benign seafloors, rippled seafloors, complex seafloors due to bathymetry and rock formations, and areas with posidonia seagrass. This provides a unique opportunity to compare the influence on performance evaluation parameters of multiple

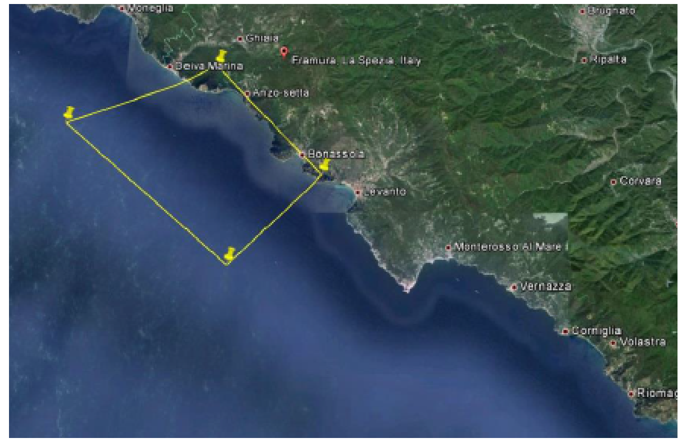

Fig. 2. The MANEX'14 trial area, located off Framura, Italy.

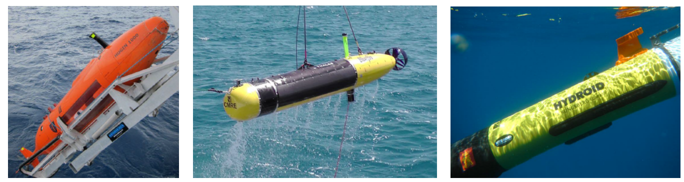

(a) (b) (c)

Fig. 3. The primary autonomous platforms employed in MANEX'14, including (a) FFI's HUGIN AUV, (b) CMRE's MUSCLE AUV, and (c) CMRE'S REMUS AUV.

sonar systems and widely varying frequencies over different seafloor areas. Typical missions were designed as a series of parallel legs in a 'lawnmower' fashion, ensuring consistent high quality sensor coverage of the seafloor. To provide a comparative dataset between the sensors, the HUGIN and MUSCLE AUVs were employed over the same areas, using consistent orientations through the use of a common set of mission waypoints. Note that the HISAS HF data were not acquired using the same waypoints, but still on nearly parallel survey lines. The REMUS, with a considerably smaller sensing range, used a different set of mission waypoints, however provided coverage over most of the seafloor areas of interest.

IV. SONAR DATA

Each sensor collects and logs data in proprietary formats, with the HUGIN and MUSCLE producing SAS tiles, and the REMUS vehicle collecting a series of 1000 pings into an 'MST' file. From these data blocks, 20 m $\times$ 20 m areas of interest were extracted using MATLAB images for analysis. In this paper we present three of these blocks for an in-depth evaluation of performance parameters across systems and frequencies. The first block covers a rippled seafloor with posidonia seagrass, the second block covers an unknown object on a rippled seafloor, while the third block covers another unknown object on the transition between a sand ripple field and benign sediment seafloor. The related sonar images are presented in the leftmost column of Figs. 4 – 6.

Details on the different sonar systems, including frequency and resolution, are presented in Table I. These sonars are not absolutely calibrated, and the reference level of the logarithmic intensity images have been chosen based on typical

TABLE I. PROPERTIES OF THE SONAR SYSTEMS AND DATA USED IN THE CURRENT STUDY

	HUGIN HISAS LF, MF & HF	**MUSCLE SAS**	**REMUS 100 Marine Sonic SSS**
Frequency	$12-38$ kHz (LF) $60-85$ kHz (MF) $85-115$ kHz (HF)	$270-330$ kHz	900 kHz
Slant range	$10-70$ m (LF) $15-75$ m (MF) $15-175$ m (HF)	$40-150$ m	$5-30$ m
Pixel Size (range $\times$ along-track)	2.0×4.0 cm (LF, MF) 4.0×4.0 cm (HF)	1.5×2.5 cm	5.9×12 cm
Theoretical resolution (range $\times$ along-track)	3.1×2.9 cm (LF, MF) 2.8×3.0 cm (HF)	1.5×2.5 cm	unknown $\times$ range dependent
Survey date	28-SEP-2015 (LF, MF) 26-SEP-2015 (HF)	22-SEP-2015	28/29-SEP-2015

background levels. The image dynamics have been chosen to show most of the variations over the scene. It is 25 dB for HISAS LF, while it is 30 dB for HISAS MF and HF as well as MUSCLE SAS. We do not know the dynamic range of the Remus 100 images.

The sonar data was logged simultaneously for HISAS LF and MF, while the survey dates for the other sensors differ by a few days. We assume temporal changes on the seafloor as small compared to differences induced by observing the blocks with various frequencies. Furthermore, please note that it was not possible to capture all areas of interest with exactly the same geometry, i.e. neither the same distance nor, in the SSS case, the same orientation.

Some general observations can be made on the frequency dependency of the sonar images:

Shadows: The shadows are darker and more prominent for the higher frequency systems. This can be related to several sources. Shadow fill-in around objects and behind the sand ripples is expected for the lowest frequency systems, where each pixel contains data from a wide range of aspect angles (90 degrees or more for HISAS LF). However, we suspect more additive noise in the shadows at the lower frequencies, as the HISAS receiver array was designed for HF. Using the same receiver array for MF and LF results in a lower sensitivity. The scattering strength is also higher for higher frequencies, which causes the shadows to appear darker. Furthermore, multipath interference will be present and is expected to be stronger at the lower frequencies, because of the wide vertical beamwidth of the prototype systems.

Bottom scattering: The relative scattering strength between benign seafloor, sand ripples and posidonia changes with frequency. This is most likely related to different scattering regimes as the ratio of wavelength to scatterer size changes. The relative higher scattering strength of sand ripples (in Fig. 6) could thus be related to different (coarser) sediments in the sand ripples than on the benign seafloor. The strong scattering from posidonia at lower frequencies (in Fig. 4) could either be a result of resonant scattering or due to a higher contribution from volume scattering within the vegetation at lower frequencies.

Object scattering: We suspect that more objects can be observed as intensity highlights at the lowest frequencies. With increasing frequency, the object intensity (relative to the bottom) decreases, and the texture becomes more important. Only the side of the object facing the sensor (broadside) reveal a glint of highlight. Because of the wide beamwidth at lower frequencies, more aspects of the object are illuminated. In addition, at the lowest frequencies the object will give internal scattering and the deeper seafloor penetration can reveal buried objects.

Sharpness: The high frequency images appear sharper than the low frequency images. In order to achieve the same theoretical resolution at low frequencies as at high frequencies, a larger relative bandwidth and a larger span of look angles must be incorporated into each pixel. The penetration depth into sediments and objects will change with relative frequency span, and combined with the wide range of look angles, this will lead to some degree of defocus of low frequency high resolution images. As more look angles are incorporated into each pixel, the low frequency imaging is also more sensitive to navigation errors when processing for a fixed resolution.

V. IMAGE QUALITY RESULTS

Comparing the HISAS and MUSCLE images, the effects of the higher frequency of the MUSCLE system can be observed in Figs. 5 and 6. The increase in frequency results in a decrease in the seafloor penetration, leading to a clearer representation of the seafloor surface itself. Furthermore, as seen in Fig. 4 with the MUSCLE system, a lower quality image is presented for the posidonia seagrass. This image is at effectively twice the range of the HISAS images, however the image illustrates an apparent defocusing over the areas of posidonia. This lower quality is reflected in the DPCA coherence values as compared to the other images in Figs. 5 and 6. The DPCA coherence plot shows a drop in the lower left corner of Fig. 4, likely caused by a large shadow following the posidonia. This effect may also be influenced by the higher frequency of the MUSCLE causing different scattering effects, however images at the same range for this sample were not available.

For a non-interferometric sidescan sonar like the Marine Sonic, there are currently no good metrics for SNR estimation available. Image contrast has been suggested, but has turned out to be scene dependent and will underestimate the SNR on benign seafloors. Multipath and surface returns can have a significant impact on the quality of the data collected for a SSS, particularly from an MCM perspective. An example of this is evident in Figs. 5 and 6, where surface returns are present in the images. The detrimental effect of the surface return on the image is particularly apparent in Fig. 5, where the highlight of the object is corrupted.

Although SSS sonar resolution will degrade with range, SSS provides high quality shadows in the image when compared to HISAS and MUSCLE, which is a key feature for object recognition for both humans and automated algorithms. As noted above, the lack of seafloor penetration allows for an accurate seafloor surface representation, however, the increased resolution cell size and the increasing nature of along track resolution with range results in a seafloor that appears more homogeneous and shows more blur than the synthetic aperture sonars. This effect can be seen through comparing the MUSCLE and SSS data in Fig. 6. In this figure, the SSS resolution can be observed changing in range, and overall texture of the

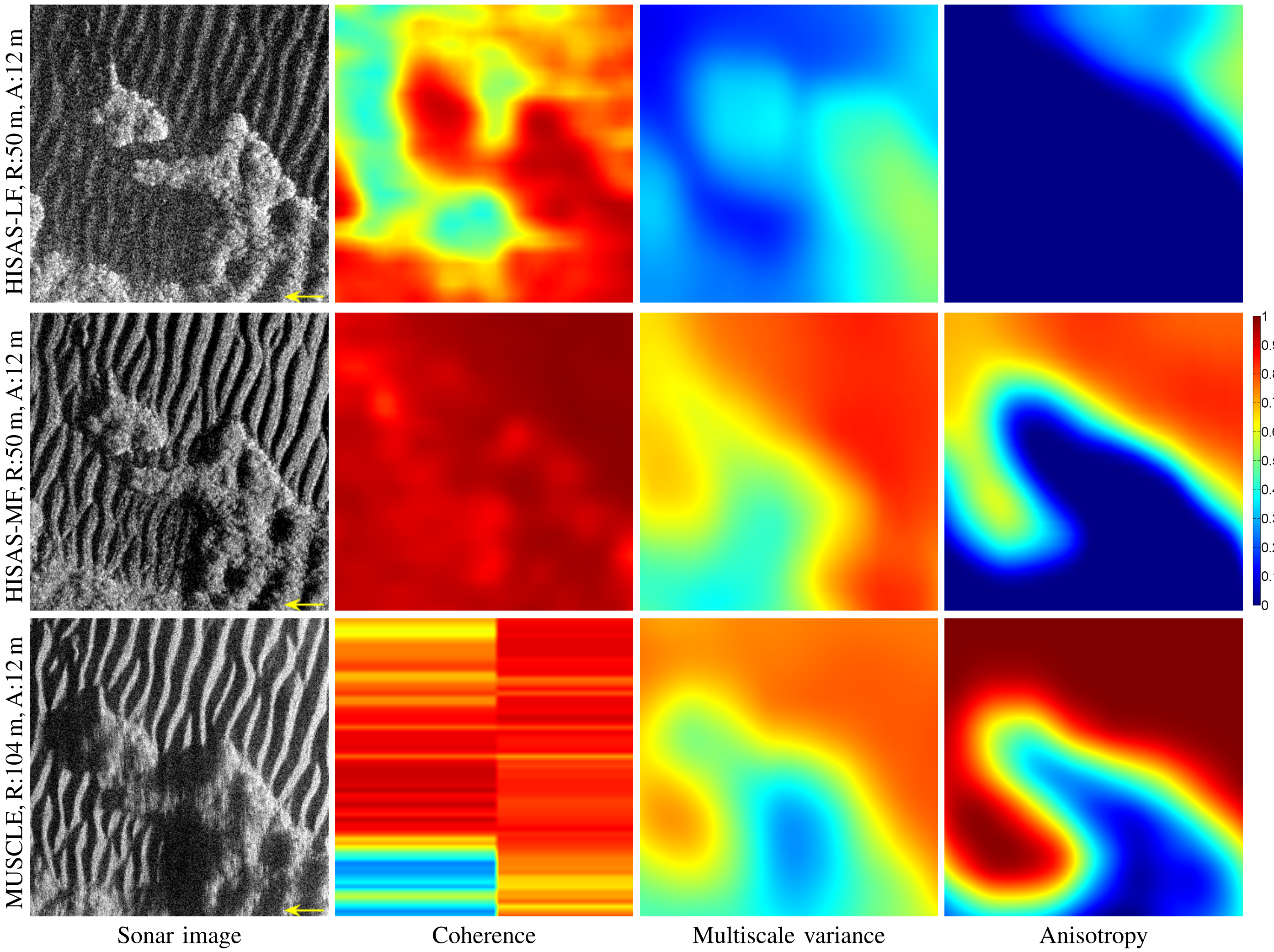

Fig. 4. Sonar images from HUGIN HUS (HISAS LF and MF) and MUSCLE of size 20 m × 20 m showing rippled seafloor with posidonia seagrass. Yellow arrows in the sonar image mark the direction from which the scene is observed. Each row label additionally contains information on the respective slant range (R) and vehicle altitude (A).

seafloor is less resolved than the MUSCLE image. Examining the MUSCLE image, the texture of the seafloor is consistent in range, one of the primary advantages of SAS processing.

From the coherence plots in Figs. 4 – 6 we can see further clear trends: HISAS HF frequency has better SNR than HISAS LF frequency. This is not surprising since HISAS was designed for the HF band and subsequently fitted with a low-end LF transmitter. It also seems like the MUSCLE temporal coherence is systematically lower than the HISAS HF interferometric coherence. This can have various causes since the sensor, the platform and the estimation algorithm all are different and thus HISAS coherence and MUSCLE coherence are not directly comparable. However, each of them may well be used in the MCM performance estimation model from Section II since the underlying performance table in the model is calibrated to image quality and image complexity obtained from the respective sensor and system equipment. The use of the DPCA values results in a coarser estimate of SNR for MUSCLE data, due to the defined ranges where the array is formed. Thin range binning of the MUSCLE coherence is most apparent in Figs. 4 and 6, where variance in the coherence values can be seen across bins. Another aspect worth noticing from the coherence plots in Figs. 4 – 6 is that due to the high resolution the HISAS coherence estimates pick up small features which can be recognized in the corresponding imagery.

VI. Image complexity results

In Figs. 4 – 6, the two rightmost columns display *multiscale variance* as well as *anisotropy* estimates for the chosen seafloor patches and sensor equipment. Firstly, focusing on *anisotropy*, we can see that it yields, as expected, particularly high values in regions of sand ripples. In Fig. 4 it is visible that *anisotropy* is largest for MUSCLE images and smallest for HISAS LF. With increasing frequency, sand ripples get more pronounced and contribute to a sharper contrast in the images. The same behavior can be seen in Figs. 5 and 6, however not for Marine Sonic SSS, which actually has the highest frequency of all sensors in this study. Here the lower resolution creates problems to capture the sand ripple patches in the *anisotropy* estimate. While it still works reasonably well in Fig. 5, it is not working well in Fig. 6, presumably due to the fact that the

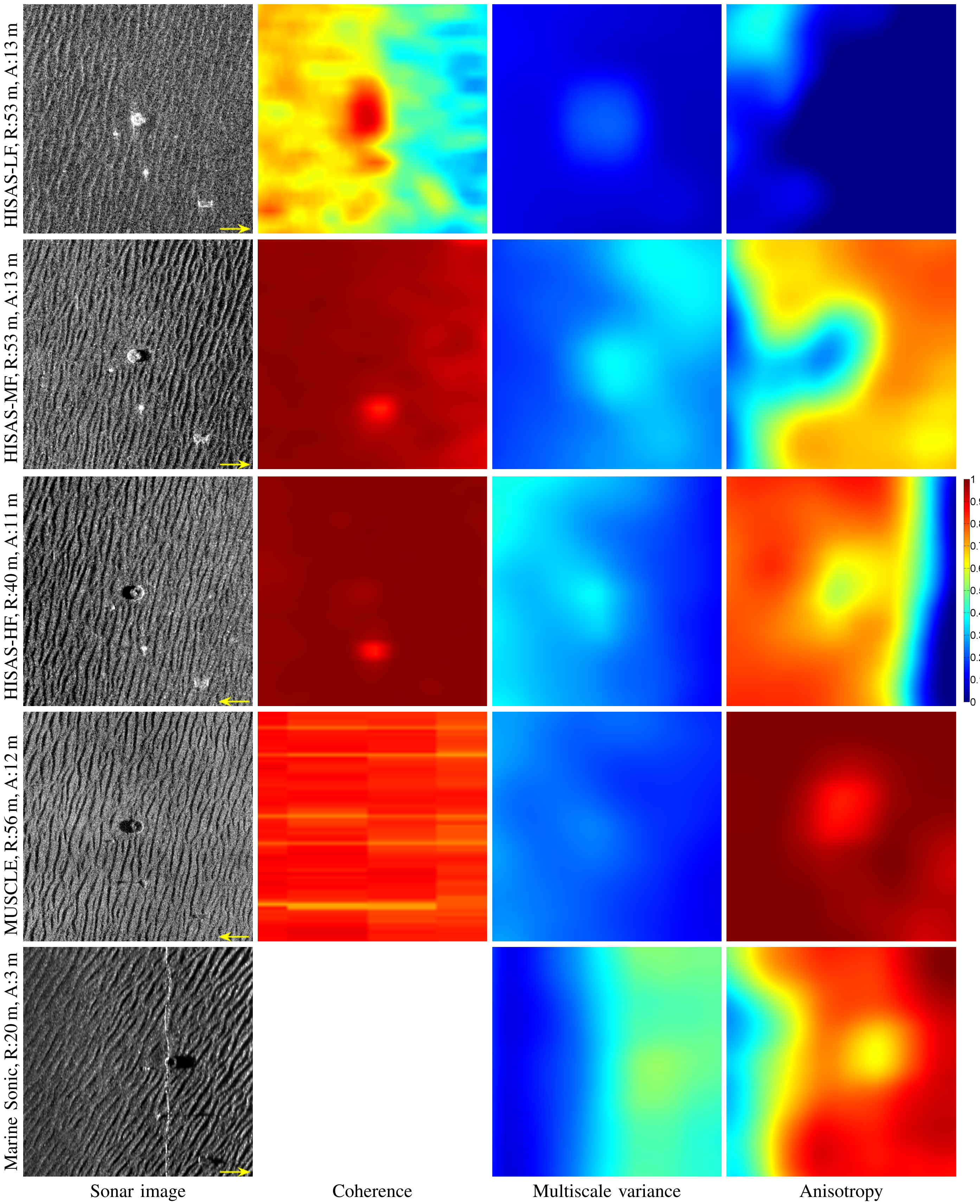

Fig. 5. Sonar images from HUGIN HUS (HISAS LF, MF and HF), MUSCLE as well as REMUS100 (Marine Sonic SSS) of size 20 m × 20 m showing an unknown object on a rippled seafloor. Yellow arrows in the sonar image mark the direction from which the scene is observed. Each row label additionally contains information on the respective slant range (R) and vehicle altitude (A).

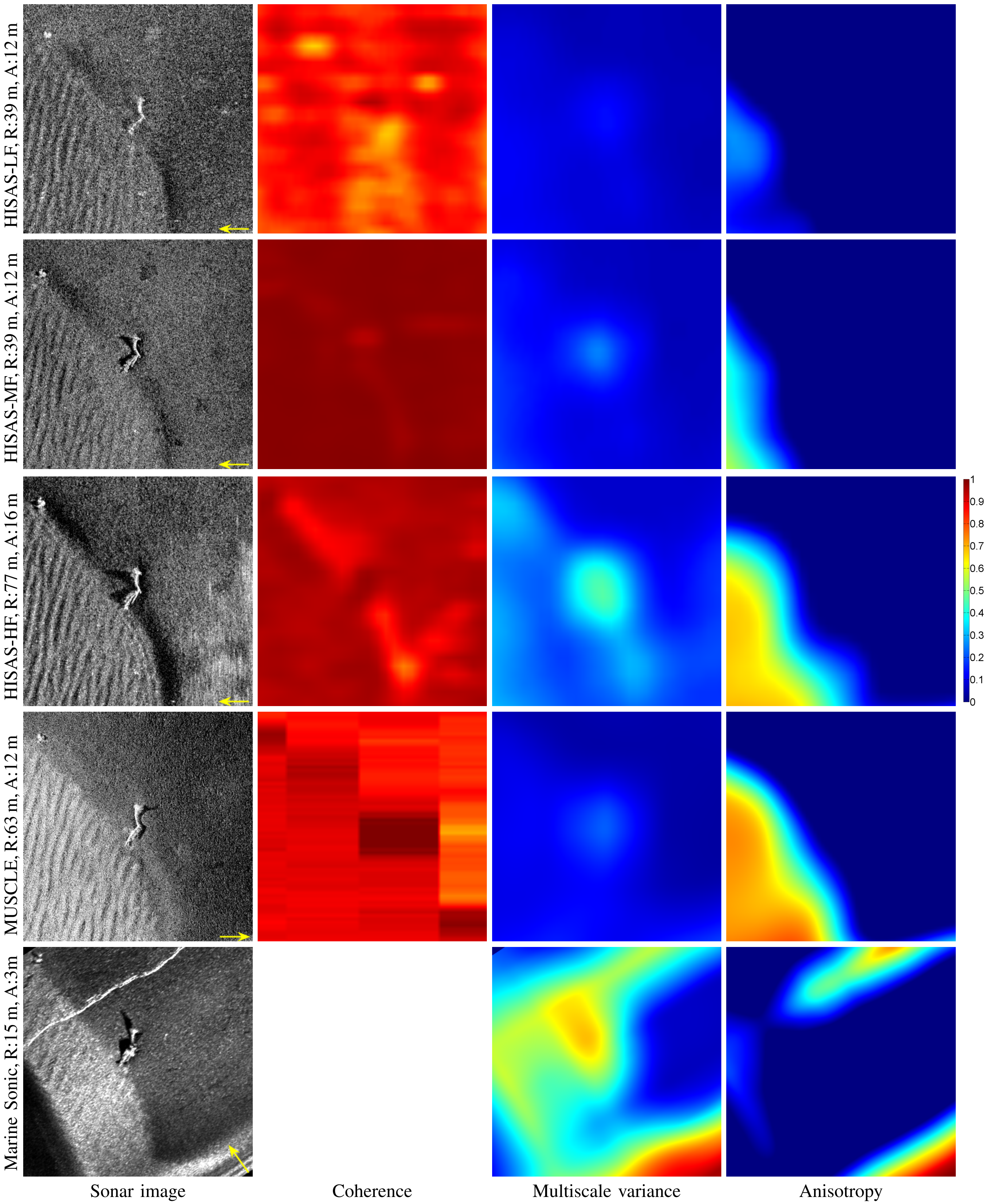

Fig. 6. Sonar images from HUGIN HUS (HISAS LF, MF and HF), MUSCLE as well as REMUS100 (Marine Sonic SSS) of size $20\,\text{m} \times 20\,\text{m}$ showing an unknown object on the transition between a sand ripple field and benign seafloor. Yellow arrows in the sonar image mark the direction from which the scene is observed. Each row label additionally contains information on the respective slant range (R) and vehicle altitude (A).

present ripples are not prominent enough in the underlying sonar image. Also the surface returns (as visible by a white line through the here shown SSS images) create problems since they show a strong directionality and thus are likely to be picked up by the *anisotropy* estimate. Another interesting point concerning *anisotropy* is the dependency on grazing angle. On a seabed with basically only sand ripples, they appear to be captured better with increasing range due to longer shadow lengths and stronger contrast between highlights and shadows, which is particularly visible in the respective images from HISAS MF, HF and Marine Sonic SSS in Fig. 5.

In Fig. 4, *multiscale variance* is mainly driven by the sand ripples for HISAS MF and MUSCLE, while in the LF case, due to absence of strong sand ripple texture, the patches of posidonia seagrass are captured by this measure, though with lower values barely exceeding 0.5. The sand ripples in Fig. 5 are on a scale smaller than mine-size, as opposed to the previous example (i.e., Fig. 4), with the effect that our *multiscale variance* estimate is rather low and generally not much influenced by the ripples. The unknown object in the center of the image contributes to our estimate, but to a rather low extent, which is as expected for just a single object, even of mine-size. Detecting a target in this environment should be fairly easy, which is reflected in the multiscale variance. The only exception appears in the Marine Sonic case, where the right half of the image features more intensity variations with increasing range than the left one, additionally triggered by the white line due to surface return of the signal. Also in Fig. 6 the ripples are of small scale, hence the observations from the previous figure are valid here as well. While the benign seafloor in the upper and right half of the image causes very low *multiscale variance* estimates as expected, the unknown object in the center causes increasing values with increasing HISAS frequency. However, this might not just be an effect of frequency alone as that object is located at a considerably larger range for HISAS HF and thus features a longer shadow. It also appears that the object is located in a small valley visible by the low intensity right in front of it seen from the viewing direction, which also could explain its short shadow (and thus low *multiscale variance*) in the MUSCLE image whose view is from the other direction. The Marine Sonic image which is observed from a very different angle features quite high *multiscale variance* estimates, where rather high values occur around the object in viewing direction, but in general the estimate is disturbed by image artifacts such as the end of the water column (lower right) and the surface return pattern (upper left).

VII. Discussion

The observations on the frequency dependency of the sonar images should be considered when designing detection and classification algorithms, and consequently also when investigating the MCM performance metrics. Our performance metrics were originally developed for the HISAS HF (100 kHz) system. When applied to the other systems and sonar frequencies, any change of importance of the different metrics must also be considered.

In contrast to the HISAS system, the estimation of the generalized SNR for MUSCLE data is through the DPCA coherence rather than interferometric coherence. From the perspective of a quality measure, each can be used to estimate a generalized SNR, as shown in [6],[19]. To produce an MCM performance metric as outlined in Section II, a performance table is used, relative to the system and threat. This allows for association between the image quality metric used for a particular system and a measured image complexity to result in a performance score calibrated to that system. This does, however, preclude any direct comparison of the coherence scores between HISAS and MUSCLE.

The CMRE Marine Sonic sonar used in this study is a real aperture sidescan sonar. From an image quality perspective, this can introduce some significant differences to estimating image quality for MCM. These differences include the measurement of resolution, the impact of vehicle motion, and estimation of SNR. The development of a SSS image quality metric for MCM is currently an open research topic, specifically generating an estimate for a generalized SNR. It should be noted however that in specific cases, such as interferometric SSS systems, an approach to estimating SNR similar to that used on the HISAS could be adopted, however the other considerations for SSS must still be accounted for. For example, vehicle motion for a SSS will have different effects on image quality than with a SAS. As the SAS depends on stable navigation and the ability to measure navigation accuracy to a high resolution, a departure from this resulting in a defocused image. For a sidescan sonar, motion artifacts are represented directly in the image, in the form of multiple pings over the same area of seafloor, or gaps in coverage. This can result in potentially missing an object detection opportunity, or distorting an object to an extent where detection or classification is impossible. As SSS image quality for MCM is still under development, the SSS data presented here does not include a calculated quality metric.

VIII. Summary

In this paper we compared data from different side-looking sonar systems acquired in a joint international effort of CMRE and FFI during the MANEX'14 sea trial. The data originates from two SAS systems (CMRE's MUSCLE and FFI's HISAS) and a real aperture SSS system, and features in total five different frequency bands with carrier frequencies ranging from 25 kHz to 900 kHz. Given FFI's suggested model for the detection and classification part of mine hunting performance estimation with its two main parameters *image quality* and *image complexity*, we demonstrated the usability of those parameters on data at different frequency bands. This was done by comparing the results for the sub-parameters *coherence*, *multiscale variance* and *anisotropy*. The presented findings suggest that the performance model can be adapted to SAS systems with frequencies different from the 100 kHz system it was designed for. With each frequency band capturing different aspects of the seafloor, the parameter values reflect the observed sonar characteristics well in the tested environments. The *image quality* parameter describes the respective sensor's ability to 'see' the seafloor and *image complexity* gives an characterization of the presence of mine-size texture in the environment seen by the sensor. Further thoughts have to be given in how to adequately fit SSS systems to FFI's MCM performance estimation model, especially with respect to deriving a metric capturing the *image quality* parameter and further adjusting the *image complexity* parameter.

ACKNOWLEDGMENT

The authors would like to thank the Captain and crew of NRV Alliance for all of their support during the MANEX'14 sea trial. Further we would like to thank NATO ACT Future Solutions for supporting CMREs research and trials program.

REFERENCES

[1] Ø. Midtgaard, I. Alm, T. O. Sæbø, M. Geilhufe, and R. E. Hansen, "Performance assessment tool for AUV based mine hunting," in *Proc. Institute of Acoustics*, vol. 36. Lerici, Italy: International Conference on Synthetic Aperture Sonar and Synthetic Aperture Radar, September 2014, pp. 120–129.

[2] S. Dugelay, D. Williams, G. Okopal, W. Connors, Ø. Midtgaard, T. Sæbø, M. Geilhufe, O. Lorentzen, M. Ditzel, S. Giodini, G. Beckers, J. Beldowski, C. Francis, A. Mannoni, M. Meltzer, P. Østenstad, and A. Hesby, "MANEX14: Experimental Description and Preliminary Results ," NATO STO Center for Marine Research and Experimentation, La Spezia, Italy, Tech. Rep. CMRE-FR-2014-013, January 2015.

[3] P. Blondel, *The Handbook of Sidescan Sonar*, ser. Geophysical Sciences. Springer Praxis Books, 2009.

[4] D. Jackson and M. Richardson, *High-Frequency Seafloor Acoustics*. Springer-Verlag, 2007.

[5] M. Geilhufe, S. Dugelay, S. A. V. Synnes, T. O. Sæbø, Ø. Midtgaard, and R. E. Hansen, "Comparative study of frequency dependency in high resolution sonar imagery from the MANEX'13 sea trials," in *Proc. Institute of Acoustics*, vol. 36. Lerici, Italy: International Conference on Synthetic Aperture Sonar and Synthetic Aperture Radar, September 2014, pp. 191–200.

[6] R. E. Hansen and T. O. Sæbø, "Towards automated performance assessment in synthetic aperture sonar," in *Proc. MTS/IEEE Oceans Europe*, Bergen, Norway, June 2013.

[7] Ø. Midtgaard, T. O. Sæbø, and R. E. Hansen, "Estimation of target detection/classification performance using interferometric sonar coherence," in *Proceedings of Underwater Acoustic Measurements 2009*, Nafplion, Greece, June 2009.

[8] T. O. Sæbø, "Seafloor depth estimation by means of interferometric synthetic aperture sonar," Ph.D. dissertation, University of Tromsø, September 2010.

[9] M. A. Pinto, "High resolution seafloor imaging with synthetic aperture sonar," *IEEE Oceanic Eng. Newsletter*, pp. 15–20, Summer 2002.

[10] A. Bellettini and M. A. Pinto, "Theoretical accuracy of synthetic aperture sonar micronavigation using a displaced phase-center antenna," *IEEE J. Oceanic Eng.*, vol. 27, no. 4, pp. 780–789, October 2002.

[11] S. A. Synnes, R. E. Hansen, and T. O. Sæbø, "Assessment of shallow water performance using interferometric sonar coherence," in *Proceedings of Underwater Acoustic Measurements 2009*, Nafplion, Greece, June 2009.

[12] M. Geilhufe and Ø. Midtgaard, "Quantifying the complexity in sonar images for MCM performance estimation," in *Proc. 2nd International Conference and Exhibition on Underwater Acoustics*, Rhodes, Greece, June 2014, pp. 1041–1048.

[13] D. B. Percival and A. T. Walden, *Wavelet Methods for Time Series Analysis*. New York, USA: Cambridge University Press, 2000.

[14] I. Daubechies, *Ten Lectures on Wavelets*, ser. Cbms-Nsf Regional Conference Series in Applied Mathematics Series. Society for Industrial and Applied Mathematics (SIAM), 1992.

[15] P. E. Hagen, T. G. Fossum, and R. E. Hansen, "HISAS 1030: The Next Generation Mine Hunting Sonar for AUVs," in *UDT Pacific 2008 Conference Proceedings*, Sydney, Australia, November 2008.

[16] S. A. V. Synnes and R. E. Hansen, "Ultra wideband SAS imaging," in *Proc. 1st International Conference and Exhibition on Underwater Acoustics*, 2013, pp. 111–118.

[17] A. Bellettini and M. A. Pinto, "Design and Experimental Results of a 300-kHz Synthetic Aperture Sonar Optimized for Shallow-Water Operations," *IEEE Journal of Oceanic Engineering*, vol. 34, no. 3, pp. 285–293, 2009.

[18] "Sea Scan PC AUV Specifications," www.marinesonic.com, 2011, Accessed: 2015-08-21.

[19] M. Couillard, J. Groen, and W. L. Fox, "Performance assessment of the muscle synthetic aperture sonar," *Proceedings of Meetings on Acoustics*, vol. 17, no. 1, 2013.